Swapping exchange and spin-orbit induced correlated phases in proximitized Bernal bilayer graphene

Yaroslav Zhumagulov,[1,*] Denis Kochan,[2,1,3,†] and Jaroslav Fabian[1,‡]
[1]*Institute for Theoretical Physics, University of Regensburg, 93040 Regensburg, Germany*
[2]*Institute of Physics, Slovak Academy of Sciences, 84511 Bratislava, Slovakia*
[3]*Center for Quantum Frontiers of Research and Technology (QFort), National Cheng Kung University, Tainan 70101, Taiwan*

(Received 6 August 2023; accepted 10 June 2024; published 15 July 2024)

Ex-so-tic van der Waals heterostructures take advantage of electrically tunable layer polarization to swap proximity exchange and spin-orbit coupling in the electronically active region. Perhaps the simplest example is Bernal bilayer graphene (BBG) encapsulated by a layered magnet from one side and a strong spin-orbit material from the other. Taking WS_2/BBG/$Cr_2Ge_2Te_6$ as a representative ex-so-tronic device, we employ realistic *ab initio* inspired Hamiltonians and effective electron-electron interactions to investigate the emergence of correlated phases within the random phase approximation. We find that exchange and spin-orbit coupling induced Stoner and intervalley coherence instabilities can be swapped for a given doping level, allowing one to explore the full spectrum of correlated phases within a single device.

DOI: 10.1103/PhysRevB.110.045427

I. INTRODUCTION

While a variety of novel electronic correlation effects have initially been discovered in twisted graphene structures [1–4], recent demonstrations of quarter- and half-metallic states [5–10] and superconductivity [7,11–17] in rhombohedral trilayer graphene, as well as the observation of isospin magnetism and spin-polarized superconductivity in Bernal bilayer graphene (BBG) [18–26], are clear evidence for correlated physics without moiré patterns. A common feature, boosting the electron-electron interactions in these systems is the presence of van Hove singularities (vHS) near the charge neutrality point [27–29]. Particularly attractive is the tunability of the correlated phases by a displacement field, which can shift the electronic levels of the vHS [5,11,18,19].

The electronic states of two-dimensional materials in van der Waals heterostructures can be also affected by proximity effects [30]. Relatively strong spin interactions, for example, can be induced in materials such as graphene which exhibits weak spin-orbit coupling [31–33]. Indeed, proximity-induced spin-orbit (SO) and exchange (EX) interactions have been predicted theoretically [34–45] and confirmed experimentally [46–60] in BBG-based heterostructures. Specifically, valley-Zeeman, Kane-Mele, and Rashba SO couplings have been shown to emerge [34–41,46–56], along with (anti)ferromagnetic EX couplings [39–43,45–57,59–61], typically causing spin splittings on the meV scale.

Perhaps the most striking manifestation of the proximity effects is the possibility to swap the spin couplings, EX and SO, by a displacement field, whereby changing the spin Hamiltonian in the active layer. This effect arises due to the interplay of the short-range proximity interactions and layer polarization by the field. An experimentally relevant materials system to consider is that of BBG encapsulated from one side by a strong spin-orbit material, such as WS_2, and a magnetic semiconductor, such as $Cr_2Ge_2Te_6$ (CGT), from the other side. The resulting heterostructure, termed "ex-so-tic" [40], allows one to imprint selectively either SO or EX coupling onto the Bloch states of the BBG.

Given that BBG can host correlated phases, is it possible to swap between the phases induced by EX and SO coupling? As we show here, ex-so-tronic devices can indeed supply on-demand correlated phases, allowing one to swap the effective single-particle excitation Hamiltonians enabled by the layer polarization effect. Although our conclusions are more general, we specifically study WS_2/BBG/CGT, for which an effective orbital and spin-interaction Hamiltonian has been derived from density functional theory (DFT) [39,40]. Employing random-phase approximation (RPA) [62–67], we first examine the particle-hole instabilities of pristine BBG, whose correlated phase diagram features intervalley coherence (IVC) [68] and Stoner instabilities [14,15]. The spin interactions induced by proximity SO (see the latest works [26,69–71]) and EX couplings remove the spin and valley degeneracies of IVC and Stoner phases and cause a plethora of emergent spin-valley correlated phases. In ex-so-tic heterostructures, such as the here employed WS_2/BBG/CGT, the phases can be effectively swapped, while the evidence of the interplay of SO and EX interactions can be seen in the single-particle [Hartree-Fock (HF)] excitation spectra which we also calculate.

II. MODEL

The orbital degrees of freedom of BBG are modeled by a realistic Bloch Hamiltonian [32,40]:

$$\hat{h}_0(\mathbf{k},\tau)=\begin{pmatrix} \Delta+V & \gamma_0 f(\mathbf{k}) & \gamma_4 f^*(\mathbf{k}) & \gamma_1 \\ \gamma_0 f^*(\mathbf{k}) & +V & \gamma_3 f(\mathbf{k}) & \gamma_4 f^*(\mathbf{k}) \\ \gamma_4 f(\mathbf{k}) & \gamma_3 f^*(\mathbf{k}) & -V & \gamma_0 f(\mathbf{k}) \\ \gamma_1 & \gamma_4 f(\mathbf{k}) & \gamma_0 f^*(\mathbf{k}) & \Delta-V \end{pmatrix} \quad (1)$$

*Contact author: iaroslav.zhumagulov@ur.de
†Contact author: denis.kochan@savba.sk
‡Contact author: jaroslav.fabian@ur.de

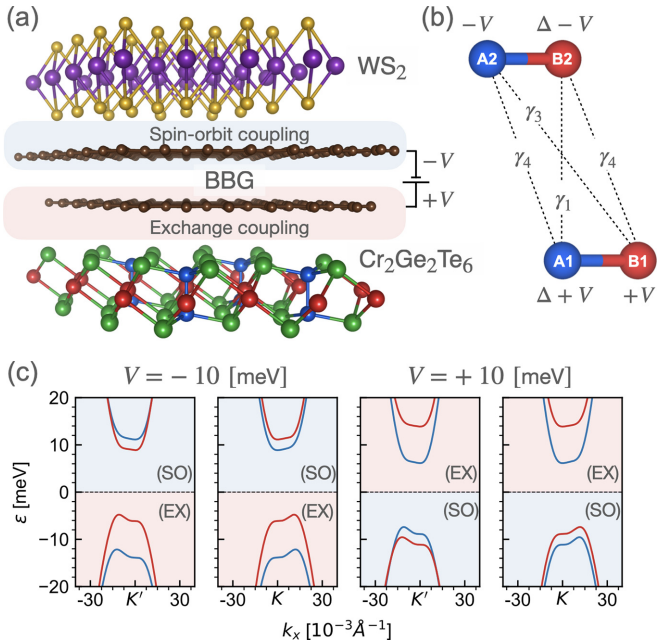

FIG. 1. (a) Scheme of an ex-so-tic heterostructure comprising of BBG encapsulated by WS_2 and CGT which proximitize the BBG by SO (WS_2) and EX (CGT) interactions. (b) BBG unit cell with relevant interlayer orbital hoppings and on-site energies. The intralayer nearest-neighbor hopping γ_0 is not indicated. The colors distinguish A and B sublattices within the two layers. (c) Calculated single-particle low-energy electronic dispersions of WS_2/BBG/CGT near K and K' points obtained from $h(\mathbf{k}, \tau)$ for $V = \pm 10$ meV; red bands are spin polarized up, blue are spin polarized down; the spin quantization axis z is perpendicular to the layers.

in the basis of p_z orbitals ordered as (A_1, B_1, A_2, B_2). Parameters γ denote intra- (γ_0) and interlayer (γ_1, γ_3, γ_4) hoppings [see Figs. 1(b) and 1(c)]. The displacement field is accounted for by on-site energy V, while the asymmetry between A and B sublattice is quantified by Δ. Momenta $\mathbf{k} = (k_x, k_y)$ are measured from K and K' valleys, while $f(\mathbf{k}) = -(\sqrt{3}a_l/2)(\tau_x - ik_y)$ is the linearized nearest-neighbor tight-binding function; $a_l = 2.46$ Å is graphene's lattice constant and $\tau = \tau_{K/K'} = \pm 1$ is the valley index. Since the SO coupling of pristine BBG is weak—about 24 μeV [32]—we do not include it in the Hamiltonian.

To model proximitized BBG in a WS_2/BBG/CGT ex-so-tic heterostructure, we need to include SO (due to WS_2) and EX (due to CGT) couplings, which were shown by *ab initio* calculations and weak-antilocalization measurements [72] to be sizable, on the order of 1 meV [39,40]. The corresponding proximity induced spin interactions are described near K and K' valleys by the Hamiltonian $\hat{h}_{\text{prox}}(\tau) = \sum_l \hat{h}^l_{\text{VZ}}(\tau) + \hat{h}^l_{\text{ex}}(\tau)$, for valley-Zeeman (VZ) spin-orbit, and exchange (ex) coupling [34,38,41,44]:

$$\hat{h}^l_{\text{VZ}}(\tau) + \hat{h}^l_{\text{ex}}(\tau) = \begin{pmatrix} \left(\tau\,\lambda^{A_l}_{\text{VZ}} - \lambda^{A_l}_{\text{ex}}\right) s_z & 0 \\ 0 & -\left(\tau\,\lambda^{B_l}_{\text{VZ}} + \lambda^{B_l}_{\text{ex}}\right) s_z \end{pmatrix}, \tag{2}$$

parametrized by the corresponding sublattice and layer-resolved couplings $\lambda^{A_l/B_l}_{\text{VZ}}$ and $\lambda^{A_l/B_l}_{\text{ex}}$. We denote by s_z the spin Pauli matrix. Each $\hat{h}^l$ is a 4×4 matrix in the spin-sublattice resolved basis $(A_{l\uparrow}, A_{l\downarrow}, B_{l\uparrow}, B_{l\downarrow})$ within layer l (bottom, $l = 1$; top, $l = 2$). Since spin-orbit coupling in graphene induced by transition metal dichalcogenide monolayers (TMDCs) is of the valley-Zeeman type [37], we set $\lambda^{A_l}_{\text{VZ}} \approx -\lambda^{B_l}_{\text{VZ}}$.

The numerical values for the parameters of the single-particle Hamiltonian, $\hat{h}(\mathbf{k}, \tau) = \hat{h}_0(\mathbf{k}, \tau) + \hat{h}_{\text{prox}}(\tau)$, are taken from the *ab initio* results of Ref. [40] and presented in Table I. The calculated low-energy band dispersions for WS_2/BBG/CGT are shown in Fig. 1(c). The signs of V and electron doping n_e determine the dominant proximity spin interaction. If both V and n_e are positive or negative, the electrons at the Fermi level experience proximity exchange coupling, while if the signs of V and n_e are opposite, the electrons at the Fermi level have strong proximity spin-orbit coupling; we use labels (SO) and (EX) in Fig. 1(c) and below when needed to keep track of the dominant spin interaction.

To investigate correlation phenomena we introduce the many-particle Hamiltonian operator as the sum of the kinetic and potential energies $\hat{H} = \hat{H}_{\text{kin}} + \hat{H}_{\text{int}}$, where

$$\hat{H}_{\text{kin}} = \sum_{\mathbf{k}\tau s,ij} \hat{c}^\dagger_{s\tau i}(\mathbf{k})[\hat{h}(\mathbf{k}, \tau) - \mu]_{si,s'j}\hat{c}_{s'\tau j}(\mathbf{k}), \tag{3}$$

$$\hat{H}_{\text{int}} = U_0(\hat{n}_{\uparrow K}\,\hat{n}_{\downarrow K} + \hat{n}_{\uparrow K'}\,\hat{n}_{\downarrow K'}) + U_1\hat{n}_K\,\hat{n}_{K'}. \tag{4}$$

Here, $\hat{c}^{(\dagger)}_{s\tau i}(\mathbf{k})$ is the annihilation (creation) operator for a Bloch electron with spin $s = \uparrow/\downarrow$ in valley $\tau = K/K'$ on BBG sublattice i with valley momentum $\mathbf{k}$; μ is the chemical potential. The intravalley and intervalley density interactions are described by repulsive (positive) couplings U_0 and U_1, respectively, while $\hat{n}_{s\tau} = \sum_{|\mathbf{k}|<k_c}\sum_i \hat{c}^\dagger_{s\tau i}(\mathbf{k})\hat{c}_{s\tau i}(\mathbf{k})$ stands for the spin-valley number operator in the $s\tau$-channel cutoff by a momentum k_c; the valley number operator then is $\hat{n}_\tau = \hat{n}_{\uparrow\tau} + \hat{n}_{\downarrow\tau}$.

In the following, we consider SU(4)-symmetric interactions by setting $U_0 = U_1 = U = 19$ eV [14,71,73], and $k_c = 0.06$ Å^{-1}, which are consistent with the experimental pristine BBG phase diagram [18,19]. We use the same interaction parameters for the WS_2/BBG/CGT heterostructure.

III. METHODOLOGY

To resolve the correlated phases of our models of pristine and proximitized BBG we employ the RPA. First, we evaluate the noninteracting generalized static Lindhard susceptibility, χ^0, [65–67] using the BBG Hamiltonian $\hat{H}_{\text{kin}}$, Eq. (3), at 0.4 K, considering different spin-valley modes $s\tau$ in the particle-hole channel. Second, we calculate the dressed susceptibility, $\chi = [1 - \chi^0\Gamma]^{-1}\chi^0$, where Γ is the irreducible vertex function corresponding to $\hat{H}_{\text{int}}$, Eq. (B2). Finally, we check for the divergence of χ: If the highest eigenvalue λ_c of $\chi^0\Gamma$ becomes greater than or equal to unity, a correlated phase corresponding to that eigenvalue emerges.

In particular, we find all possible correlated phases $\hat{\Phi}$ of different spin-valley channels by first diagonalizing $\chi^0\Gamma$ at $\mu = 0$ and $V = 0$. Then, varying the doping and displacement field, we compute the corresponding χ^0 and $\chi^0\Gamma$. For each $\hat{\Phi}$ found above we estimate the critical parameter $\lambda_c(\hat{\Phi}) = \langle\hat{\Phi}|\chi^0\Gamma|\hat{\Phi}\rangle/\|\hat{\Phi}\|^2$. The dominant instability is realized by phase $\hat{\Phi}$ that at given μ and V has the highest $\lambda_c(\hat{\Phi})$. Each

TABLE I. The numerical values for the parameters of the low-energy single-particle Hamiltonian of WS_2/BBG/CGT heterostructure are taken from the *ab initio* results of Ref. [40].

γ_0 (eV)	γ_1 (eV)	γ_3 (eV)	γ_4 (eV)	Δ (meV)	$\lambda_I^{A_2}$ (meV)	$\lambda_I^{B_2}$ (meV)	$\lambda_X^{A_1}$ (meV)	$\lambda_X^{B_1}$ (meV)
2.432	0.365	−0.273	−0.164	8.854	1.132	−1.132	−3.874	3.874

symmetry-breaking phase $\hat{\Phi}$ can be expressed in terms of $\hat{c}^{(\dagger)}_{s\tau i}(\mathbf{k})$ operators:

$$\hat{\Phi} = \sum_{|\mathbf{k}|<k_c} \sum_i \hat{c}^{\dagger}_{s\tau i}(\mathbf{k}) \, [\, M_\Phi \,]_{s\tau,s'\tau'} \, \hat{c}_{s'\tau' i}(\mathbf{k}), \tag{5}$$

where the spin-valley resolved matrices M_Φ that are relevant for our model are listed in Table II. However, at the phase boundaries, the dominant phase can be unresolved due to the degeneracy of several $\lambda_c(\hat{\Phi})$.

Figure 2 displays the obtained correlated phase diagram of pristine BBG. We find IVC and Stoner instabilities, as also reported earlier [14,15]. While the Stoner instability is local, the IVC state corresponds to a phase spatially modulated by wave vector $\mathbf{q}$ which connects K and K' valleys. The fact that $\hat{H}_{\text{kin}}$ lacks particle-hole symmetry is reflected in the different phases for the electron and hole doping ranges. Both IVC and Stoner phases exhibit degeneracies, as listed in Table I, due to not fully broken spin-valley symmetries. The critical temperatures for each correlated phase depend heavily on the doping parameters and displacement field. With the chosen interaction parameters, it can reach up to 2.2 K for IVC and 1.0 K for the Stoner phases, as shown in Appendix E.

Figure 3 shows the main result of the paper. There, we plot the correlated phase diagram of WS_2/BBG/CGT for different doping levels and displacement fields. Compared with the pristine case, the phase diagram of proximitized BBG is rather rich. Indeed, if the Fermi level crosses bands experiencing strong proximity SO coupling, the Stoner phase breaks up into two $\text{SVP}_\pm$ states—both displaying spin-valley polarization along the $\pm z$ direction—while IVC splits into spin-valley coherent states $\text{SVC}_\pm$. Resolving specific spin-valley states within the Stoner and IVC phases is attributed to the valley-Zeeman SO coupling [37]. Similarly, if the Fermi level lies in bands with strong EX coupling, the Stoner phase evolves into valley-polarized states, $\text{VP}_\pm$, while IVC is split into charge density waves, $\text{VC}_\pm$. The multitude of spin-valley-split phases of proximitized BBG due to SO and EX interactions are summarized in Table II, including the explicit forms of the phase operators $\hat{\Phi}$. Their expectation values in the corresponding ground states can serve as the conventional order parameters discriminating different phases.

Let us take a closer look at vHS. If the singularity is split due to the valley-Zeeman SO coupling, two $\text{SVC}_\pm$ phases appear. As the corresponding $M_{\text{SVC}_\pm}$ contain spin s_x and s_y matrices, and valley τ_x and τ_y matrices, they can be described as intervalley spin-flip hopping that retains the spin-valley quantum number, i.e., the product of $s\tau$. Say, spin up at K is degenerate with spin down at K'. Coupling the two enabled by the Coulomb interaction lowers the kinetic energy, resulting in an SVC correlated phase. Similarly, when vHS are split by EX interaction, two spin-polarized $\text{VC}_\pm$ phases form up. Contrary to $\text{SVC}_\pm$, $M_{\text{VC}_\pm}$ does not mix spins—it involves s_0 and s_z spin matrices—but similarly as $\text{SVC}_\pm$ it intertwines the valleys—matrix τ_x. Because of that both $\text{SVC}_\pm$ and $\text{VC}_\pm$ possess spatial modulations; the correlations effectively enlarge the BBG unit cell into a "magnetic" 3×3 unit cell. Consequently, the Brillouin zone gets smaller while both valleys fold into the Γ point. In what follows, the $\mathbf{k}$ vector is measured with respect to the center of such a reduced Brillouin zone.

Finally, to find the effective single-particle excitation energies of the correlated phases of our WS_2/BBG/CGT model, we employ the HF method and solve the following eigenproblem:

$$(\hat{H}_{\text{kin}} + \hat{\Sigma})|\tilde{u}_n(\mathbf{k})\rangle = \tilde{\varepsilon}_{n\mathbf{k}}|\tilde{u}_n(\mathbf{k})\rangle, \tag{6}$$

where $\tilde{\varepsilon}_{n\mathbf{k}}$ and $|\tilde{u}_n(\mathbf{k})\rangle$ are HF-corrected quasiparticle energies and wave functions labeled by the band index n and the $\mathbf{k}$ vector in the reduced Brillouin zone. Correspondingly, $\hat{\Sigma}$ represents the HF self-energy, which mixes spin and valley indices; for details, see Appendix C.

To illustrate how our ex-so-tic heterostructure enables one to swap two correlated phases, one induced by valley-Zeeman SO and the other by EX coupling, we consider one particular doping level, namely hole density $n_e = -0.183 \times 10^{12}$ cm^{-2}. At positive $V = 18.5$ meV, the most stable correlated phase (largest λ_c) is a spin-valley coherence SVC_-. This phase arises due to the proximity spin-orbit coupling from WS_2, and couples the opposite spins at the two valleys. It is characterized by the flat band states close to the Fermi level exhibiting reduced spin polarization, which is not exactly zero because of the residual proximity exchange. Flipping the direction of the displacement field to $V = -18.5$ meV, a different correlated

TABLE II. List of phases and corresponding phase operators $\hat{\Phi} = \sum_{|\mathbf{k}|<k_c} \sum_i \hat{c}^{\dagger}_{s\tau i}(\mathbf{k}) \, [\, M_\Phi \,]_{s\tau,s'\tau'} \, \hat{c}_{s'\tau' i}(\mathbf{k}) = \hat{\Phi}^{\dagger}$ resolved in different spin-valley channels for the relevant symmetry-broken phases of pristine and proximitized BBG. The spin-valley resolved matrices M_Φ entering $\hat{\Phi}$'s are given in the third line. Phases involving τ_x or τ_y are valley mixed, i.e., they possess spatial modulation with vector $\mathbf{q} = (2\pi/3a_l)(1, \sqrt{3})$ which connects K and K' valleys.

Pristine BBG phases	IVC		Stoner	
Proximity phases	$\text{SVC}_\pm$	$\text{VC}_\pm$	$\text{SVP}_\pm$	$\text{VP}_\pm$
Spin-valley matrices M_Φ	$[s_x\tau_x \pm s_y\tau_y]$	$[s_0 \pm s_z]\tau_x$	$[s_z\tau_0 \pm s_0\tau_z]$	$[s_0 \pm s_z]\tau_z$

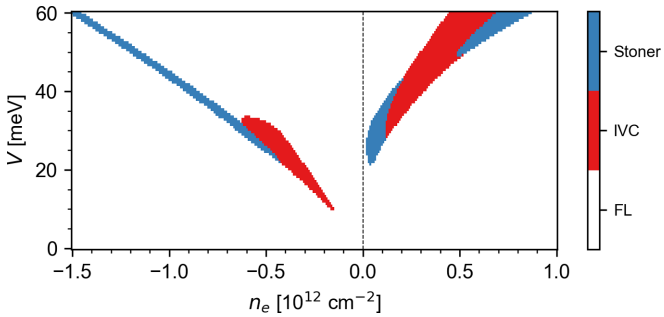

FIG. 2. Calculated phase diagram of pristine BBG for varying doping n_e and displacement field V. We only show phases for $V > 0$, as the diagram has V to $-V$ symmetry. There are two dominant phases: the intervalley coherent phase (IVC), displayed by blue, and the Stoner instability, shown in red. The white background corresponds to a stable Fermi liquid (FL). The phase diagram was obtained for $T = 0.4$ K.

phase emerges, VC$_-$, in which the states at the Fermi level are fully spin polarized, due to the proximity exchange from CGT.

In Fig. 4 we also show the markedly different quasiparticle Fermi contours of the two swappable phases SVC$_-$ and VC$_-$. To make this visualization, we plotted the thermally broadened density of states (derivative of the Fermi-Dirac function) at $T = 0.4$ K:

$$\rho_{n\mathbf{k}} = -\left.\frac{df(\varepsilon)}{d\varepsilon}\right|_{\tilde{\varepsilon}_{n\mathbf{k}}} = \frac{1}{k_B T}\left[4\cosh\left(\frac{\tilde{\varepsilon}_{n\mathbf{k}} - \mu}{2k_B T}\right)\right]^{-2}. \quad (7)$$

Inspecting Fig. 4 we see that the quasiparticle band structures for the two considered phases, and also the shapes of their Fermi contours, demonstrate very pronounced spectral asymmetries at the corresponding Fermi levels. However, regions with more smeared portions of the Fermi surface (different from just contour plots) are visible in the center of the reduced Brillouin zone.

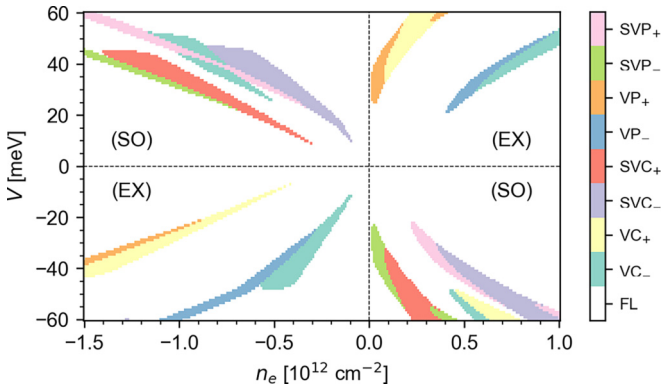

FIG. 3. (a) Correlated-phase diagram of a model of ex-so-tic WS$_2$/BBG/CGT heterostructure, for varying doping n_e and displacement field V. Eight symmetry-breaking phases are predicted to emerge due to the interplay of the electron-electron interactions and proximity-induced SO and EX splittings: VC$_\pm$ (valley coherence), SVC$_\pm$ (spin-valley coherence), SVP$_\pm$ (spin-valley polarized state), and VP$_\pm$ (valley polarized state), each marked by a different color. The FL phase is displayed by white. The phase diagram was obtained for $T = 0.4$ K.

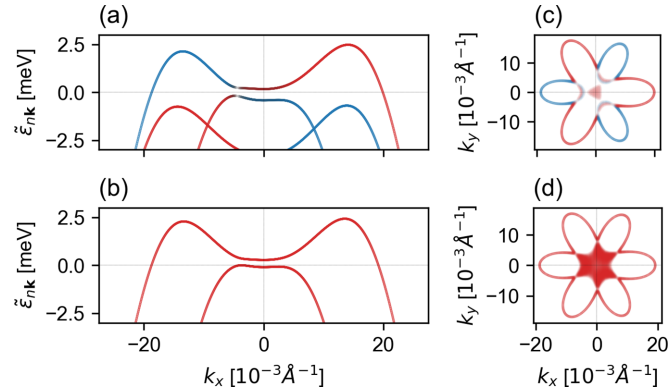

FIG. 4. Swapping SVC and VC. Calculated HF quasiparticle band structures and spin-valley-resolved Fermi surfaces for the correlated SVC$_-$ phase (a), (c), with $V = +18.5$ meV and $n_e = -0.183 \times 10^{12}$ cm^{-2}, and VC$_-$ phase (b), (d), with $V = -18.5$ meV and $n_e = -0.183 \times 10^{12}$ cm^{-2}. Red, blue, and gray lines mark, correspondingly, spin-up, spin-down, and spin-unpolarized states.

Knowing the HF self-energies $\hat{\Sigma}$ we are able to estimate the magnitudes of the associated correlated gaps, $\Delta_{\hat{\Phi}} = \sum_{s\tau,s'\tau'} \hat{\Phi}^*_{s'\tau',s\tau} \hat{\Sigma}_{s\tau,s'\tau'}/\|\hat{\Phi}\|^2$. This yields for the considered SVP$_-$ and VC$_-$ phases the following values: $\Delta_{\text{SVP}_-} = 0.109$ meV and $\Delta_{\text{VC}_-} = 0.085$ meV.

To model an interacting system with a symmetry-broken phase at a self-consistent mean-field level, one can factorize $\hat{H}_{\text{int}}$, Eq. (B2), in terms of accessible $\hat{\Phi}$'s and for a given dominant phase approximate the interaction just by $\hat{H}_\Delta = \Delta_{\hat{\Phi}}\hat{\Phi}$. For example, for a SVC$_\pm$ phase, one explores an effective Hamiltonian $\hat{H}_{\text{kin}} + \Delta_{\text{SVC}_\pm}\hat{\Phi}_{\text{SVC}_\pm}$ which promotes spin-flip-valley-flip hopping due to the interplay of intervalley electron-electron interactions and the valley-Zeeman SO coupling. Such a phase enables alternative spin interactions and is expected to result in alternative phenomena in spintronics [74]. In turn, a VC$_\pm$ phase can be treated on the mean-field level by $\hat{H}_{\text{kin}} + \Delta_{\text{VC}_\pm}\hat{\Phi}_{\text{VC}_\pm}$ which gives rise to spatial modulations of the already spin-split bands due to the proximity-induced EX interaction.

IV. CONCLUSION

By performing realistic calculations at the RPA level, and by computing Hartree-Fock excitation spectra, we predict that the correlated states of ex-so-tic heterostructures based on BBG can be swapped between SO and EX driven phases. A single device can exhibit the full spectrum of correlated phases, from uniform Stoner valley polarized, to spatially modulated spin-polarized VC and spin-flip-valley-flip spin-valley coherences. While we specifically consider the DFT parametrization of one stacking of WS$_2$/BBG/CGT, our findings are more general and valid for twisted structures with modified proximity spin interactions, as well as for different encapsulating spin-orbit materials and magnetic semiconductors/insulators.

ACKNOWLEDGMENTS

This work was funded by the Deutsche Forschungsgemeinschaft (German Research Foundation) SPP 2244 (Project

No. 443416183), SFB 1277 (Project No. 314695032), by the European Union Horizon 2020 Research and Innovation Program under Contract No. 881603 (Graphene Flagship), and by FLAG-ERA project 2DSOTECH. D.K. acknowledges partial support from IMPULZ Project No. IM-2021-26—SUPERSPIN funded by the Slovak Academy of Sciences.

APPENDIX A: GENERALIZED LINDHARD SUSCEPTIBILITY TENSOR

To calculate the static susceptibility tensor, χ^0_{abcd}, we use the generalized Lindhard susceptibility formula that employs the eigenstates and eigenvalues of the full single-particle Hamiltonian $\hat{h}_{\tau s}(\mathbf{k})$, in the case of pristine or proximitized BBG, correspondingly, with or without the proximity-furnished SO and EX interactions:

$$\sum_j \hat{h}^a_{ij}(\mathbf{k}) u^{aj}_{n\mathbf{k}} = \varepsilon^a_{n\mathbf{k}} u^{ai}_{n\mathbf{k}}, \tag{A1}$$

where $\varepsilon^a_{n\mathbf{k}}$ denotes single-particle energy and $u^{ai}_{n\mathbf{k}}$ is the amplitude of the nth eigenstate $|u_{n\mathbf{k}}\rangle$ projected onto a sublattice i in a spin-valley channel a. In what follows we reserve indices m, n to label electronic bands stemming from the single-particle Hamiltonian $\hat{h}(\mathbf{k})$, and indices i, j to label BBG sublattices (A_1, B_1, A_2, B_2). Moreover, we introduce four quantum numbers 0,1,2,3—saddled by indices a, b, c, d, u, v—that overall parametrize the spin-valley degrees of freedom:

$$\begin{aligned} 0 &= (\uparrow \times K), 1 = (\uparrow \times K'), \\ 2 &= (\downarrow \times K), 3 = (\downarrow \times K'). \end{aligned} \tag{A2}$$

Also, we would like to point out that indices with a bar such as $\bar{a}, \bar{b}$, etc., correspond to creation operators, while those without a bar such as a, b, etc., correspond to annihilation operators.

The generalized Lindhard susceptibility tensor, χ^0, can be given in terms of eigenenergies $\varepsilon^a_{n\mathbf{k}}$ and projections $u^{ai}_{n\mathbf{k}}$ as follows:

$$\begin{aligned} \chi^0_{\bar{a}b\bar{b}a} = A_{uc} \int_{|\mathbf{k}|<k_c} \frac{d^2\mathbf{k}}{(2\pi)^2} \\ \times \sum_{nm} \sum_{ij} \frac{f^a_{n\mathbf{k}} - f^b_{m\mathbf{k}}}{\varepsilon^b_{m\mathbf{k}} - \varepsilon^a_{n\mathbf{k}}} \left(u^{ai}_{n\mathbf{k}}\right)^* u^{bi}_{m\mathbf{k}} \left(u^{bj}_{m\mathbf{k}}\right)^* u^{aj}_{n\mathbf{k}}, \end{aligned} \tag{A3}$$

where A_{uc} stands for an area of the unit cell and the corresponding Fermi-Dirac weights $f^a_{n\mathbf{k}}$ read

$$f^a_{n\mathbf{k}} = \frac{1}{1 + \exp\left[\left(\varepsilon^a_{n\mathbf{k}} - \mu\right)/k_B T\right]} \tag{A4}$$

where μ is chemical potential.

The static susceptibility, χ^0, as used in the main text and below is computed for $T = 0.4$ K (equivalent in energy to 0.02 meV, which is an order of magnitude below the magnitudes of all estimated correlated gaps $\Delta_{\hat{\Phi}}$), and for the momentum cutoff $k_c = 0.06$ Å^{-1}. The latter corresponds to the orbital-energy scale $\sqrt{3}/2 a_l \gamma_0 k_c = 0.453$ eV, i.e., the employed ultraviolet cutoff is sufficiently larger than the SO and EX coupling strengths, displacement field magnitudes, and chemical potentials as considered in this paper. This proves that the used temperature T and electron-electron couplings U_0 and U_1 are chosen meaningfully and are not spoiling the physical results obtained in our calculations.

APPENDIX B: RANDOM PHASE APPROXIMATION: VERTEX FUNCTION

We treat emergent correlations by means of the following density-density Hamiltonian:

$$\begin{aligned} \hat{H}_{\text{int}} &= U_0(n_{\uparrow K} n_{\downarrow K} + n_{\uparrow K'} n_{\downarrow K'}) + U_1 n_K n_{K'} \\ &= U_0(n_0 n_2 + n_1 n_3) + U_1(n_0 + n_2)(n_1 + n_3) \end{aligned} \tag{B1}$$

where $U_0 > 0$ and $U_1 > 0$ are parametrizing the intravalley and intervalley effectively repulsive interactions. To obtain the RPA vertex function, U, we use the conventional approach, which gives

$$\hat{H}_{\text{int}} = \frac{1}{4} \sum_{abcd} U_{c\bar{a}d\bar{b}} \hat{c}^\dagger_{\bar{a}} \hat{c}^\dagger_{\bar{b}} \hat{c}_c \hat{c}_d. \tag{B2}$$

The representative components of this spin-valley tensor are given by

$$\begin{aligned} U_{0220} = U_{1331} &= +U_0, \\ U_{0022} = U_{1133} &= -U_0, \\ U_{0110} = U_{0330} = U_{1221} = U_{2332} &= +U_1, \\ U_{0011} = U_{0033} = U_{1122} = U_{2233} &= -U_1. \end{aligned} \tag{B3}$$

All nonprovided components of the U tensor can be obtained by the relation $U_{abcd} = U_{dcba}$.

APPENDIX C: SELF-CONSISTENT HARTREE-FOCK CALCULATIONS

This paper employed a self-consistent Hartree-Fock approach to determine the correlated band structure. The effective Schrödinger equation is given by

$$\sum_b \left[\varepsilon^a_{n\mathbf{k}} \delta_{\bar{a}b} + \Sigma_{\bar{a}b}\right] \tilde{u}^b_{n\mathbf{k}} = \tilde{\varepsilon}_{n\mathbf{k}} \tilde{u}^a_{n\mathbf{k}}, \tag{C1}$$

where $\tilde{\varepsilon}^a_{n\mathbf{k}}$ and $\tilde{u}_{n\mathbf{k}}$ denote Hartree-Fock corrected single-particle energy and wave function, and as before n denotes band index and a, b are spin-valley degrees of freedom. Σ_{ab} is the Hartree-Fock self-energy that was calculated as follows:

$$\Sigma_{\bar{a}b} = -\sum_{cd} U_{b\bar{a}c\bar{d}} G_{c\bar{d}}, \tag{C2}$$

where U_{abcd} is the RPA vertex function and G_{cd} is the density matrix. The density matrix is subsequently determined as follows:

$$G_{c\bar{d}} = A_{uc} \int_{|\mathbf{k}|<k_c} \frac{d^2\mathbf{k}}{(2\pi)^2} \sum_{i,n} \left[\tilde{f}_{n\mathbf{k}} - \frac{1}{2}\right] \tilde{u}^{ci}_{n\mathbf{k}} \left(\tilde{u}^{di}_{n\mathbf{k}}\right)^*. \tag{C3}$$

Note that the orbital and band indices are traced out to calculate the density matrix G_{cd}. The corresponding Fermi-Dirac weights $\tilde{f}_{n\mathbf{k}}$ read

$$\tilde{f}_{n\mathbf{k}} = \frac{1}{1 + \exp[(\tilde{\varepsilon}_{n\mathbf{k}} - \mu)/k_B T]}. \tag{C4}$$

We constrain chemical potential μ by fixing electron doping:

$$n_e = \int_{|\mathbf{k}|<k_c} \frac{d^2\mathbf{k}}{(2\pi)^2} \sum_n \left[\tilde{f}_{n\mathbf{k}} - \frac{1}{2}\right]. \tag{C5}$$

The offset $-1/2$ in Eqs. (C3) and (C5) is intended to fix the chemical potential equal to zero at the point of charge neutrality.

APPENDIX D: TWO-PARTICLE RESPONSE FUNCTION LINEAR ALGEBRA

In our paper, we used the following linear algebra rule for the product of two-particle response functions in a particle-hole channel labeled by the spin-valley indices:

$$[A \cdot B]_{abcd} = \sum_{uv} A_{abuv} B_{vucd}. \tag{D1}$$

Thus, the expression for calculating the critical parameter can be obtained as follows:

$$\lambda_c = \frac{1}{\|\hat{\Phi}\|^2} \sum_{ab} \sum_{cd} \hat{\Phi}^*_{b\bar{a}} \chi^0_{\bar{a}b\bar{b}a} U_{a\bar{b}c\bar{d}} \hat{\Phi}_{\bar{d}c}. \tag{D2}$$

The most relevant set of $\hat{\Phi}$'s corresponding to correlated phases in BBG with and without SO and EX couplings was obtained by the diagonalization of the symmetric matrix $\chi^0 U$:

$$\lambda_c \hat{\Phi}_{\bar{a}b} = \sum_{cd} \chi^0_{\bar{a}b\bar{b}a} U_{a\bar{b}c\bar{d}} \hat{\Phi}_{\bar{d}c}, \tag{D3}$$

at charge neutrality point and zero displacement field. The list of $\hat{\Phi}$'s is provided in Table II in the main text.

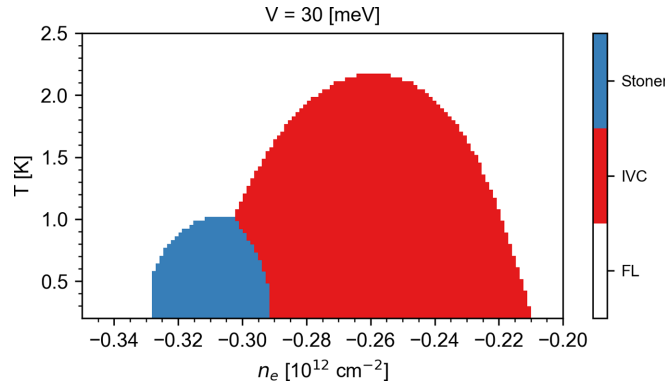

FIG. 5. Temperature/doping phase diagram for pristine BBG at the displacement field with a layer energy difference of 30 meV. There are two dominant phases: the IVC, displayed by blue, and the Stoner instability, shown in red. The white background corresponds to a FL.

The value of the correlated gap in our paper was calculated using the following formula:

$$\Delta_{\hat{\Phi}} = \frac{1}{\|\hat{\Phi}\|^2} \sum_{ab} \hat{\Phi}^*_{b\bar{a}} \Sigma_{\bar{a}b}. \tag{D4}$$

Prefactor $1/\|\hat{\Phi}\|^2$ is due to the normalization of $\hat{\Phi}$, as represented in Table II in the main text.

APPENDIX E: TEMPERATURE/DOPING PHASE DIAGRAM FOR PRISTINE BBG

To clarify the robustness of the different phases with temperature, we calculated a temperature/doping phase diagram for pristine BBG at the fixed displacement field $V = 30$ meV, which is displayed in Fig. 5. The Stoner phase is predicted to be stable up to 1.0 K, while IVC can be up to 2.2 K.

[1] C. R. Dean, L. Wang, P. Maher, C. Forsythe, F. Ghahari, Y. Gao, J. Katoch, M. Ishigami, P. Moon, M. Koshino, T. Taniguchi, K. Watanabe, K. L. Shepard, J. Hone, and P. Kim, Nature (London) **497**, 598 (2013).

[2] Y. Kim, P. Herlinger, P. Moon, M. Koshino, T. Taniguchi, K. Watanabe, and J. H. Smet, Nano Lett. **16**, 5053 (2016).

[3] Y. Cao, V. Fatemi, S. Fang, K. Watanabe, T. Taniguchi, E. Kaxiras, and P. Jarillo-Herrero, Nature (London) **556**, 43 (2018).

[4] Y. Cao, V. Fatemi, A. Demir, S. Fang, S. L. Tomarken, J. Y. Luo, J. D. Sanchez-Yamagishi, K. Watanabe, T. Taniguchi, E. Kaxiras, R. C. Ashoori, and P. Jarillo-Herrero, Nature (London) **556**, 80 (2018).

[5] H. Zhou, T. Xie, A. Ghazaryan, T. Holder, J. R. Ehrets, E. M. Spanton, T. Taniguchi, K. Watanabe, E. Berg, M. Serbyn, and A. F. Young, Nature (London) **598**, 429 (2021).

[6] A. L. Szabó and B. Roy, Phys. Rev. B **105**, L081407 (2022).

[7] D.-C. Lu, T. Wang, S. Chatterjee, and Y.-Z. You, Phys. Rev. B **106**, 155115 (2022).

[8] C. Huang, T. M. R. Wolf, W. Qin, N. Wei, I. V. Blinov, and A. H. MacDonald, Phys. Rev. B **107**, L121405 (2023).

[9] F. Winterer, F. R. Geisenhof, N. Fernandez, A. M. Seiler, F. Zhang, and R. T. Weitz, Nat. Phys. **20**, 422 (2024).

[10] F. R. Geisenhof, F. Winterer, A. M. Seiler, J. Lenz, T. Xu, F. Zhang, and R. T. Weitz, Nature (London) **598**, 53 (2021).

[11] H. Zhou, T. Xie, T. Taniguchi, K. Watanabe, and A. F. Young, Nature (London) **598**, 434 (2021).

[12] Y.-Z. Chou, F. Wu, J. D. Sau, and S. Das Sarma, Phys. Rev. Lett. **127**, 187001 (2021).

[13] A. Ghazaryan, T. Holder, M. Serbyn, and E. Berg, Phys. Rev. Lett. **127**, 247001 (2021).

[14] Y.-Z. You and A. Vishwanath, Phys. Rev. B **105**, 134524 (2022).

[15] S. Chatterjee, T. Wang, E. Berg, and M. P. Zaletel, Nat. Commun. **13**, 6013 (2022).

[16] T. Cea, P. A. Pantaleón, V. T. Phong, and F. Guinea, Phys. Rev. B **105**, 075432 (2022).

[17] W. Qin, C. Huang, T. Wolf, N. Wei, I. Blinov, and A. H. MacDonald, Phys. Rev. Lett. **130**, 146001 (2023).

[18] H. Zhou, L. Holleis, Y. Saito, L. Cohen, W. Huynh, C. L. Patterson, F. Yang, T. Taniguchi, K. Watanabe, and A. F. Young, Science **375**, 774 (2022).

[19] Y. Zhang, R. Polski, A. Thomson, É. Lantagne-Hurtubise, C. Lewandowski, H. Zhou, K. Watanabe, T. Taniguchi, J. Alicea, and S. Nadj-Perge, Nature (London) **613**, 268 (2023).

[20] A. M. Seiler, F. R. Geisenhof, F. Winterer, K. Watanabe, T. Taniguchi, T. Xu, F. Zhang, and R. T. Weitz, Nature (London) **608**, 298 (2022).

[21] Y.-Z. Chou, F. Wu, J. D. Sau, and S. Das Sarma, Phys. Rev. B **105**, L100503 (2022).

[22] S. C. de la Barrera, S. Aronson, Z. Zheng, K. Watanabe, T. Taniguchi, Q. Ma, P. Jarillo-Herrero, and R. Ashoori, Nat. Phys. **18**, 771 (2022).

[23] L. Holleis, C. L. Patterson, Y. Zhang, H. M. Yoo, H. Zhou, T. Taniguchi, K. Watanabe, S. Nadj-Perge, and A. F. Young, Ising superconductivity and nematicity in Bernal bilayer graphene with strong spin orbit coupling, arXiv:2303.00742.

[24] A. L. Szabó and B. Roy, Phys. Rev. B **105**, L201107 (2022).

[25] Y.-Z. Chou, F. Wu, and S. Das Sarma, Phys. Rev. B **106**, L180502 (2022).

[26] M. Xie and S. Das Sarma, Phys. Rev. B **107**, L201119 (2023).

[27] G. Li, A. Luican, J. M. B. L. dos Santos, A. H. C. Neto, A. Reina, J. Kong, and E. Y. Andrei, Nat. Phys. **6**, 109 (2010).

[28] R. Bistritzer and A. H. MacDonald, Proc. Natl. Acad. Sci. USA **108**, 12233 (2011).

[29] F. Zhang, B. Sahu, H. Min, and A. H. MacDonald, Phys. Rev. B **82**, 035409 (2010).

[30] J. F. Sierra, J. Fabian, R. K. Kawakami, S. Roche, and S. O. Valenzuela, Nat. Nanotechnol. **16**, 856 (2021).

[31] M. Gmitra, S. Konschuh, C. Ertler, C. Ambrosch-Draxl, and J. Fabian, Phys. Rev. B **80**, 235431 (2009).

[32] S. Konschuh, M. Gmitra, D. Kochan, and J. Fabian, Phys. Rev. B **85**, 115423 (2012).

[33] S. Konschuh, M. Gmitra, and J. Fabian, Phys. Rev. B **82**, 245412 (2010).

[34] M. Gmitra, D. Kochan, and J. Fabian, Phys. Rev. Lett. **110**, 246602 (2013).

[35] A. López, L. Colmenárez, M. Peralta, F. Mireles, and E. Medina, Phys. Rev. B **99**, 085411 (2019).

[36] T. Naimer, K. Zollner, M. Gmitra, and J. Fabian, Phys. Rev. B **104**, 195156 (2021).

[37] M. Gmitra and J. Fabian, Phys. Rev. B **92**, 155403 (2015).

[38] M. Gmitra, D. Kochan, P. Högl, and J. Fabian, Phys. Rev. B **93**, 155104 (2016).

[39] K. Zollner and J. Fabian, Phys. Rev. B **104**, 075126 (2021).

[40] K. Zollner, M. Gmitra, and J. Fabian, Phys. Rev. Lett. **125**, 196402 (2020).

[41] K. Zollner, M. Gmitra, and J. Fabian, Phys. Rev. B **105**, 115126 (2022).

[42] K. Zollner, M. Gmitra, T. Frank, and J. Fabian, Phys. Rev. B **94**, 155441 (2016).

[43] H. Haugen, D. Huertas-Hernando, and A. Brataas, Phys. Rev. B **77**, 115406 (2008).

[44] D. Kochan, S. Irmer, and J. Fabian, Phys. Rev. B **95**, 165415 (2017).

[45] K. Zollner and J. Fabian, Phys. Rev. Lett. **128**, 106401 (2022).

[46] J. H. Garcia, M. Vila, A. W. Cummings, and S. Roche, Chem. Soc. Rev. **47**, 3359 (2018).

[47] J. O. Island, X. Cui, C. Lewandowski, J. Y. Khoo, E. M. Spanton, H. Zhou, D. Rhodes, J. C. Hone, T. Taniguchi, K. Watanabe, L. S. Levitov, M. P. Zaletel, and A. F. Young, Nature (London) **571**, 85 (2019).

[48] A. M. Hoque, D. Khokhriakov, K. Zollner, B. Zhao, B. Karpiak, J. Fabian, and S. P. Dash, Commun. Phys. **4**, 124 (2021).

[49] T. S. Ghiasi, J. Ingla-Aynés, A. A. Kaverzin, and B. J. van Wees, Nano Lett. **17**, 7528 (2017).

[50] T. S. Ghiasi, A. A. Kaverzin, P. J. Blah, and B. J. van Wees, Nano Lett. **19**, 5959 (2019).

[51] C. K. Safeer, J. Ingla-Aynés, F. Herling, J. H. Garcia, M. Vila, N. Ontoso, M. R. Calvo, S. Roche, L. E. Hueso, and F. Casanova, Nano Lett. **19**, 1074 (2019).

[52] F. Herling, C. K. Safeer, J. Ingla-Aynés, N. Ontoso, L. E. Hueso, and F. Casanova, APL Mater. **8**, 071103 (2020).

[53] T. Wakamura, F. Reale, P. Palczynski, M. Q. Zhao, A. T. C. Johnson, S. Guéron, C. Mattevi, A. Ouerghi, and H. Bouchiat, Phys. Rev. B **99**, 245402 (2019).

[54] T. Wakamura, N. J. Wu, A. D. Chepelianskii, S. Guéron, M. Och, M. Ferrier, T. Taniguchi, K. Watanabe, C. Mattevi, and H. Bouchiat, Phys. Rev. Lett. **125**, 266801 (2020).

[55] J. Ingla-Aynés, F. Herling, J. Fabian, L. E. Hueso, and F. Casanova, Phys. Rev. Lett. **127**, 047202 (2021).

[56] A. A. Kaverzin, T. S. Ghiasi, A. H. Dismukes, X. Roy, and B. J. van Wees, 2D Mater. **9**, 045003 (2022).

[57] B. Karpiak, A. W. Cummings, K. Zollner, M. Vila, D. Khokhriakov, A. M. Hoque, A. Dankert, P. Svedlindh, J. Fabian, S. Roche, and S. P. Dash, 2D Mater. **7**, 015026 (2020).

[58] A. G. Rybkin, A. A. Rybkina, M. M. Otrokov, O. Y. Vilkov, I. I. Klimovskikh, A. E. Petukhov, M. V. Filianina, V. Y. Voroshnin, I. P. Rusinov, A. Ernst, A. Arnau, E. V. Chulkov, and A. M. Shikin, Nano Lett. **18**, 1564 (2018).

[59] D. Marchenko, A. Varykhalov, J. Sánchez-Barriga, O. Rader, C. Carbone, and G. Bihlmayer, Phys. Rev. B **91**, 235431 (2015).

[60] A. Varykhalov, D. Marchenko, J. Sánchez-Barriga, M. R. Scholz, B. Verberck, B. Trauzettel, T. O. Wehling, C. Carbone, and O. Rader, Phys. Rev. X **2**, 041017 (2012).

[61] M. Peralta, E. Medina, and F. Mireles, Phys. Rev. B **99**, 195452 (2019).

[62] D. Bohm and D. Pines, Phys. Rev. **82**, 625 (1951).

[63] D. Pines and D. Bohm, Phys. Rev. **85**, 338 (1952).

[64] D. Bohm and D. Pines, Phys. Rev. **92**, 609 (1953).

[65] K. Kuroki, S. Onari, R. Arita, H. Usui, Y. Tanaka, H. Kontani, and H. Aoki, Phys. Rev. Lett. **101**, 087004 (2008).

[66] S. Graser, T. A. Maier, P. J. Hirschfeld, and D. J. Scalapino, New J. Phys. **11**, 025016 (2009).

[67] T. A. Maier, S. Graser, P. J. Hirschfeld, and D. J. Scalapino, Phys. Rev. B **83**, 100515(R) (2011).

[68] K. Nomura, S. Ryu, and D.-H. Lee, Phys. Rev. Lett. **103**, 216801 (2009).

[69] T. Wang, M. Vila, M. P. Zaletel, and S. Chatterjee, Phys. Rev. Lett. **132**, 116504 (2024).

[70] J. M. Koh, J. Alicea, and E. Lantagne-Hurtubise, Phys. Rev. B **109**, 035113 (2024).

[71] Y. Zhumagulov, D. Kochan, and J. Fabian, Phys. Rev. Lett. **132**, 186401 (2024).

[72] J. Amann, T. Völkl, T. Rockinger, D. Kochan, K. Watanabe, T. Taniguchi, J. Fabian, D. Weiss, and J. Eroms, Phys. Rev. B **105**, 115425 (2022).

[73] Y.-Z. You and A. Vishwanath, npj Quantum Mater. **4**, 16 (2019).

[74] I. Žutić, J. Fabian, and S. Das Sarma, Rev. Mod. Phys. **76**, 323 (2004).